This article has been accepted for publication in a future issue of this journal, but has not been fully edited. Content may change prior to final publication. Citation information: DOI 10.1109/TAP.2018.2866989, IEEE Transactions on Antennas and Propagation

Direction of Arrival Estimation Using Amplitude and Phase Information in Low-profile MIMO Arrays

Hui Li, *Member, IEEE*, Sining Sun, and Jie Wang, *Member, IEEE*

Accurate direction of arrival (DOA) estimation in compact terminal devices using small antenna arrays is challenging due to their limited radiating apertures. In this work, we employ both the amplitude and the phase information to improve the estimation accuracy and eliminate phase ambiguity without increasing the size of the antenna array. The optimal amplitude ratio between the antenna patterns is theoretically studied using the theories of Fisher information, Cramér-Rao bound and ambiguity function. Criteria of proper amplitude ratio are summarized from the theoretical investigations. Following the guidelines, two antenna arrays are modified to build effective antenna patterns and improve the estimation accuracy. Specifically, the compact monopole-patch array and the dual-monopole array reduce the DOA estimation errors by over 60% and 20-40%, respectively, under a medium SNR of 10 dB. The phase ambiguity has been eliminated in both arrays as well. The monopole-patch array requires phase calibration in the measurement, whereas the dual-monopole array does not. Experiments were carried out for the dual-monopole array in the anechoic chamber, achieving the estimation accuracy of 0.67^{o} averaged over 360^{o} .

***Index Terms*—Direction of arrival (DOA) estimation; direction finding; compact antenna array; multiple signal classification (MuSiC); MIMO antenna system**

I. Introduction

Smart low-profile portable devices enabled with localization function become a trend in the future, for both civil and military applications [1]. The limited volume of the devices confines the radiation aperture of the antenna array inside, and thus brings challenges for accurate direction of arrival (DOA) estimation. Conventionally, antenna arrays utilize phase information to find the DOA, with each element separated by around half wavelength for reliable estimations [2]. With the linear arrays, phase ambiguity exists, and the estimation accuracy is limited at the end-fire directions, especially for the arrays with fewer antenna elements in terminal devices. The mutual coupling between the antenna elements also deteriorates the estimation accuracy, which is normally compensated using mutual coupling matrix [3], [4].

Beside phase information, amplitude comparison is another widely used method for direction finding [5]-[9]. In this case, the radiation patterns of the antenna normally vary greatly over a wide frequency spectrum, and the DOA is estimated by correlating the received signal over a broad band with the calibrated amplitude pattern at different angles. The angle giving the highest correlation is determined as the arriving angle. Wideband antennas, such as ESPAR antenna [5], log-periodic antenna [6], horn antenna [7] and planar ultra wideband monopole [8], are frequently used for the amplitude-based estimation. As single antenna is sufficient in the amplitude-based method, the estimation system is usually compact. However, this method is normally limited to high SNR scenarios and merely applies to a certain range of angles.

To improve the estimation accuracy, investigations were carried out to get benefit from both the amplitude and the phase information [10]-[14]. [12] studied the effect of antenna directivity on the DOA estimation using uniform circular arrays, showing that patch antennas provide more accurate estimation as opposed to dipole antennas. Electrically small antenna system comprised of two loops and one dipole was demonstrated to achieve a 6° estimation accuracy in [13]. However, it is a three dimensional structure, and only applies to high SNR scenarios with SNR > 20 dB. Inspired by human ears, absorber was introduced to break the symmetry of the antennas and induce amplitude difference over angles. This way, the phase ambiguity has been eliminated and the estimation error has been improved by 2° - 3° [14]. Yet the antennas were separated by several wavelengths, and the absorber had a side effect that it reduced the signal power received by the antennas and thus equivalently lowered the SNR in practice. To the best of the authors' knowledge, neither effort has been made on theoretically obtaining the appropriate antenna amplitude patterns for DOA estimations, nor the antenna geometries have been shaped for this purpose.

In this work, we aim at providing guidelines for improving the DOA estimation accuracy in compact terminal devices in perspective of antenna pattern design. Dual-antenna arrays are built practically according to the criteria. In section II, theoretical studies, including the Cramér-Rao bound (CRB) and the ambiguity function, are carried out to get the optimal amplitude ratio between the antenna patterns, with the guidelines summarized for the practical antenna design. Afterwards, two antenna arrays, including a monopole-patch array and a dual-monopole array, are designed to build appropriate amplitude ratios by structure modifications. The design procedures and the improved estimation accuracy are demonstrated in details in section III. Finally, the dual-monopole array was fabricated, with its direction finding ability verified experimentally in section IV. Section V concludes the paper.

II. Theoretical Study of Steering Vector

This section firstly investigates how to choose the appropriate amplitude ratio function for dual-antenna arrays based upon the theories of Fisher information and CRB. Then the derived amplitude ratio is validated to improve the estimation accuracy measured by ambiguity function and root mean square (RMS) errors.

A. Cramér-Rao bound

For a dual-antenna array shown in the inset of Fig. 1, the steering vector using only the phase information is expressed as:

Manuscript received Mar 24th, 2018. This work was supported partly by: (1) National natural science foundation of China (no. 61601079); (2) Natural science foundation of Liaoning province (no. 20170540169).

H. Li, S. Sun and J. Wang are with School of Information and Communication Engineering, Dalian University of Technology, Dalian, 116024, China. E-mail: hui.li@dlut.edu.cn.

This article has been accepted for publication in a future issue of this journal, but has not been fully edited. Content may change prior to final publication. Citation information: DOI 10.1109/TAP.2018.2866989, IEEE Transactions on Antennas and Propagation

$$\mathbf{A}_0(\theta)=\left[1 \quad e^{\frac{-j2\pi d\sin\theta}{\lambda}}\right]^T. \tag{1}$$

The phase difference between the signals received by the two antennas, i.e., $\frac{2\pi d\sin\theta}{\lambda}$, is depicted in Fig. 1 for $d=0.45\lambda$. As is known, the phase difference is indistinguishable for the arriving angles θ and $180^\circ-\theta$. The other behavior seen from the curve is that its slope becomes smaller when θ approaches $\pm 90^\circ$. As a result, the resolution of the phase difference is low at the end-fire directions, leading to larger DOA estimation errors.

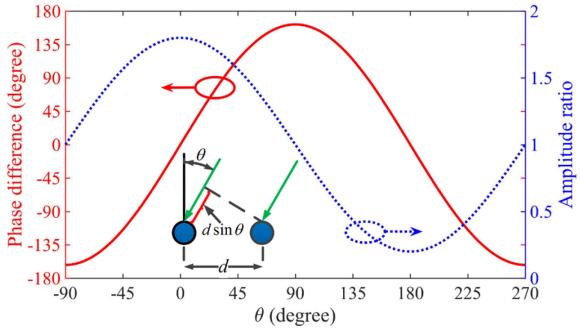

Fig. 1. Phase difference (red solid line) and amplitude ratio (blue dashed line) versus arriving angle θ.

To improve the estimation accuracy at the end-fire directions and eliminate the phase ambiguity, amplitude information is employed, and the steering vector is changed to:

$$\mathbf{A}(\theta)=\left[\alpha_1(\theta) \quad \alpha_2(\theta)e^{\frac{-j2\pi d\sin\theta}{\lambda}}\right]^T, \tag{2}$$

where $\alpha_1(\theta)$ and $\alpha_2(\theta)$ are the amplitudes of the radiation patterns for the two antennas, which are the functions of the arriving angle θ. We choose the amplitude ratio $R=\alpha_2(\theta)/\alpha_1(\theta)$ between the antennas to be with the form of $1+\sum_{i=1}^{+\infty}m_i(\cos\theta)^i$ because 1) it is a periodic function like the sine function exhibited by the phase difference in Fig. 1; 2) it has the largest slope at the end-fire directions, which is complementary to the sine function; 3) it makes sure that the ratio averaged over all the angles equals to one, indicating the same amount of power received by the two antennas.

Considering the realization of the amplitude ratio using practical antennas, we investigate the basic form of the ratio function and express it as:

$$R=1+m\cos\theta,\ m\in(-1,1). \tag{3}$$

The range of m guarantees that the ratio is always positive.

Following the amplitude ratio R in (3), we look for the optimal m using the theories of Fisher information and CRB. The steering vector $\mathbf{A}(\theta,m)$ and its first partial derivative $\mathbf{A}_1(\theta,m)$ with respect to θ are expressed as:

$$\mathbf{A}(\theta,m)=\left[1 \quad (1+m\cos\theta)e^{\frac{-j2\pi d\sin\theta}{\lambda}}\right]^T, \tag{4}$$

$$\mathbf{A}_1(\theta,m)=\left[0 \quad (-m\sin\theta-j(1+m\cos\theta)(\frac{2\pi d}{\lambda}\cos\theta))e^{\frac{-j2\pi d\sin\theta}{\lambda}}\right]^T. \tag{5}$$

According to the models in [15] and [16], the signals received by a dual-antenna array can be denoted as:

$$\mathbf{x}=\rho\mathbf{A}(\theta,m)+\mathbf{n}, \tag{6}$$

where ρ is the complex transmitted signal and $\mathbf{n}$ is the zero-mean Gaussian white noise. With this model, the probability density function $f(\mathbf{x}|\theta,m)$ and its natural logarithm $l(\mathbf{x}|\theta,m)$ are represented as [15]:

$$f(\mathbf{x}|\theta,m)=Ce^{-(\mathbf{x}-\rho\mathbf{A}(\theta,m))^H\mathbf{R}^{-1}(\mathbf{x}-\rho\mathbf{A}(\theta,m))}, \tag{7}$$

$$\begin{aligned} l(\mathbf{x}|\theta,m)&=\ln f(\mathbf{x}|\theta,m)\\ &=\ln C-(\mathbf{x}-\rho\mathbf{A}(\theta,m))^H\mathbf{R}^{-1}(\mathbf{x}-\rho\mathbf{A}(\theta,m)) \end{aligned}. \tag{8}$$

C is the normalization constant and $\mathbf{R}=\sigma^2\mathbf{I}$ is the covariance matrix of the Gaussian noise.

The Fisher information $I(\theta,m)$ is then calculated as :

$$\begin{aligned} I(\theta,m)&=\mathrm{E}_{\mathbf{x}}[(l'(\mathbf{x}|\theta,m))^2]=-\mathrm{E}_{\mathbf{x}}[l''(\mathbf{x}|\theta,m)]\\ &=\frac{2a^2}{\sigma^2}\mathbf{A}_1^H(\theta,m)\mathbf{A}_1(\theta,m) \end{aligned}, \tag{9}$$

where $l'(\mathbf{x}|\theta,m)$ and $l''(\mathbf{x}|\theta,m)$ are the first and second partial derivatives of $l(\mathbf{x}|\theta,m)$ with respect to θ, and

$$\begin{aligned} \mathbf{A}_1^H(\theta,m)\mathbf{A}_1(\theta,m)&=[(\sin\theta)^2+\frac{4\pi^2d^2}{\lambda^2}(\cos\theta)^4]m^2\\ &+\frac{8\pi^2d^2}{\lambda^2}(\cos\theta)^3m+\frac{4\pi^2d^2}{\lambda^2}(\cos\theta)^2 \end{aligned}. \tag{10}$$

According to the theory of CRB, the variance of the estimated parameter $\hat{\theta}$ is bounded by the reciprocal of the Fisher information, that is:

$$\mathrm{var}(\hat{\theta},m)\geq\frac{1}{I(\theta,m)}. \tag{11}$$

Thus, reducing the CRB is equivalent to increasing $I(\theta,m)$. Accordingly, our goal for finding out the optimal m is equivalent to maximizing the smallest $I(\theta,m)$, when θ is changing from 0° to 360°. It is mathematically expressed as:

$$\tilde{m}=\arg\max_m\{\min_\theta\{I(\theta,m)\}\} \quad m\in(-1,1). \tag{12}$$

Since the coefficient $2a^2/\sigma^2$ in (9) is always positive, (12) is equivalent to

$$\tilde{m}=\arg\max_m\{\min_\theta\{\mathbf{A}_1^H(\theta,m)\mathbf{A}_1(\theta,m)\}\} \quad m\in(-1,1). \tag{13}$$

Obtaining the analytical results based on (10) and (13) is difficult. Instead, we employ numerical methods to solve the problem in (13). It follows two steps: firstly, we set a fixed m, and calculate $\mathbf{A}_1^H(\theta,m)\mathbf{A}_1(\theta,m)$ versus θ, with its minimum value denoted. Secondly we sweep over m in (-1,1), and search for the m that corresponds to the maximum value among the noted minimum values. During the calculation, the step widths of 0.001 and 0.05° are set for m and θ, respectively.

Fig. 2(a) presents the distribution of $\mathbf{A}_1^H(\theta,m)\mathbf{A}_1(\theta,m)$ for m=0.1, 0.611 and 0.825, respectively, with the mutual distance of $d=0.25\lambda$. The minimum value in each curve is marked by the arrow. It is observed that two local minima appear at around 90° and 270°, corresponding to the poor estimation accuracy at those end-fire directions. Then we sweep m from -1 to 1 to obtain the individual minimum value, and find out the optimal m by seeking the maximum point from the curve in Fig. 2(b). This way, the smallest $I(\theta,m)$ is maximized. According to (10), the optimal m is also related to the mutual distance d between the two antennas. In our study, three mutual distances, i.e., $d=0.25\lambda,0.28\lambda,0.45\lambda$, are taken into consideration,

This article has been accepted for publication in a future issue of this journal, but has not been fully edited. Content may change prior to final publication. Citation information: DOI 10.1109/TAP.2018.2866989, IEEE Transactions on Antennas and Propagation

whose optimal m values are found to be $\pm 0.611, \pm 0.637, \pm 0.738$, respectively.

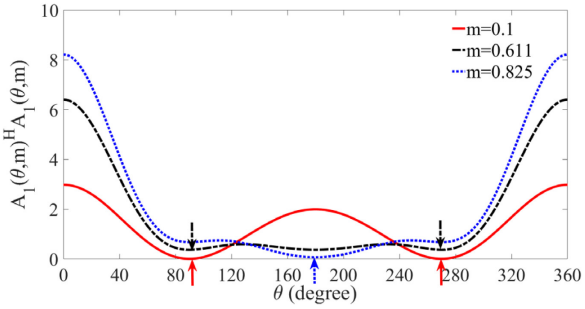

(a)

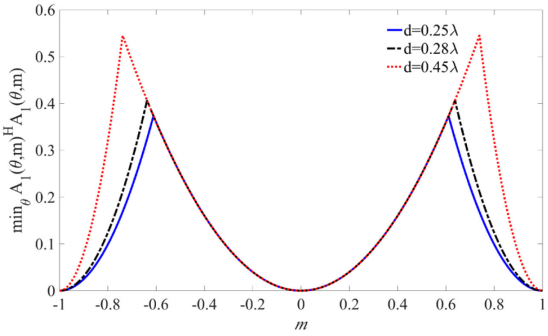

(b)

Fig. 2. (a) The distribution of $\mathbf{A}_1^H(\theta,m)\mathbf{A}_1(\theta,m)$ versus θ for m=0.1, 0.611 and 0.825. (b) The distribution of $\min_\theta \mathbf{A}_1^H(\theta,m)\mathbf{A}_1(\theta,m)$ versus m.

The RMS errors are studied for the dual antennas with different amplitude ratios using multiple signal classification (MuSiC) algorithm. The distance between the antennas is set to be 0.25λ. The calculation is carried out for a reference SNR of 10 dB. For each angle, the RMS error is calculated over 30 estimations, with each estimation based on 1500 realizations. The results are presented in Fig. 3. The case with m=0 corresponds to the estimation with only the phase information. Due to the phase ambiguity of the m=0 case, the RMS error is merely calculated for the upper half space (black solid line) and mirrored to the lower half space (black dashed line) in the figure, in order to provide intuitive comparison over 360° arriving angles.

Fig. 3 shows that the estimation accuracy is greatly improved when proper amplitude information is employed, especially at around 90° and 270°. In addition, it is evident that compared to the ratio with $m = \pm 0.611$, the RMS errors for the case of m=0.825 are larger near 180°. This can be explained by the Fisher information curve in Fig. 2(a), where the global minimum appears at 180° for the m=0.825 case. This observation indicates the relationship between smaller Fisher information and lower estimation accuracy.

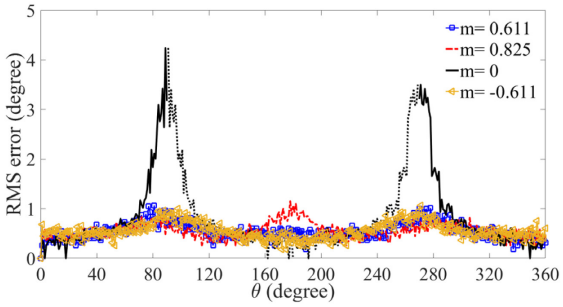

Fig. 3. RMS errors for the dual-antenna arrays with different amplitude ratios under the SNR of 10 dB for d= 0.25λ.

B. *Ambiguity function*

Ambiguity function, proposed by Erić *et al* [17], is one of the appropriate tools to measure the similarity between the steering vectors. It is defined as the normalized inner product of two steering vectors:

$$\chi_{i,j} = \frac{\mathbf{A}^H(\theta_i)\mathbf{A}(\theta_j)}{\|\mathbf{A}(\theta_i)\| \cdot \|\mathbf{A}(\theta_j)\|}. \tag{14}$$

$\chi_{i,j} = 1$ means that the two steering vectors are identical, resulting in indistinguishable arriving angles. Contrarily, when $\chi_{i,j}$ is small, it is easy to distinguish two arriving angles correctly. In this study, we calculate the ambiguity function between the steering vectors around the end-fire directions, with a step of $\Delta\theta$=5°. The absolute values of $\chi_{i,j}$ for $d = 0.45\lambda$ are presented in Fig. 4, for m=0 and m=0.738, respectively. The diagonal elements of $\chi_{i,j}$ are equal to 1 for both cases as it is the self-correlation. For the m=0 case, the back-diagonal elements are also equal to 1 due to the phase ambiguity as illustrated before. Comparatively, the back-diagonal elements of $\chi_{i,j}$ are reduced for m=0.738, indicating that the steering vectors for θ and $180^\circ - \theta$ can be distinguished. As a result, the phase ambiguity is eliminated. The smaller $\chi_{i,j}$ for the m=0.738 case implies the increased estimation resolution around the end-fire directions.

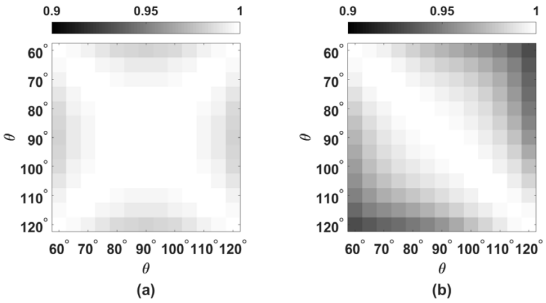

(a) (b)

Fig. 4. The absolute values of $\chi_{i,j}$ for the steering vectors with the amplitude ratios of (a) m=0; (b) m=0.738.

From antenna design perspective, it is not possible to exactly fulfill the optimal amplitude ratio with practical antennas. However, guidelines can be provided based on the above analysis. The appropriate ratio R needs to satisfy the following criteria: 1) it can provide enough asymmetry over the $\theta = \pm 90^\circ$ plane to eliminate the phase ambiguity; 2) its slope should be large at around $\pm 90^\circ$; 3) its magnitude should fall in a reasonable range for better estimation accuracy at medium SNR scenarios.

III. Antenna Design

For practical antenna designs in this section, the radiation patterns are shaped and optimized for the $\varphi = 0^\circ$ plane (*xoz* plane), on which the DOA estimation is carried out. Attentions are also paid to the amplitude ratios at other φ planes, and it is observed that most of the amplitude ratios satisfy the guidelines concluded from the theoretical studies in section II. But those amplitude ratios are not specially optimized.

A. *Monopole-patch Array*

Monopole and dipole antennas are conventionally used for DOA estimations for their simplicity. Ideally, both of the antenna types have omni-directional patterns, meaning that the amplitude is the same for all the arriving angles on the $\varphi = 0^\circ$ plane. Patch antenna, by contrast,

This article has been accepted for publication in a future issue of this journal, but has not been fully edited. Content may change prior to final publication. Citation information: DOI 10.1109/TAP.2018.2866989, IEEE Transactions on Antennas and Propagation

has a boresight radiation pattern of similar shape as the cosine function in (3). In view of this, a previous work using dipole and patch array was carried out in [18], with the estimation accuracy improved. Considering the necessity of balun for dipole antennas, in this work, we use monopole antenna instead to further reduce the size of the array.

The geometries of the compact monopole-patch array are shown in Fig. 5. Both antennas are printed on Rogers RO4003C substrate with a permittivity of 3.48 and a thickness of 1.524 mm. The mutual distance between the two antennas is 35 mm, corresponding to 0.28λ. An L-shaped ground plane is utilized. To control the amplitude ratio conveniently, a ring slot is etched in the ground plane right below the patch to tune its backward radiation. Besides, adjusting the size of the ground plane can also change the amount of backward radiation of the patch antenna. As a result, the radiation pattern of the patch antenna exhibits proper asymmetry regarding the θ=90° plane (*xoy* plane).

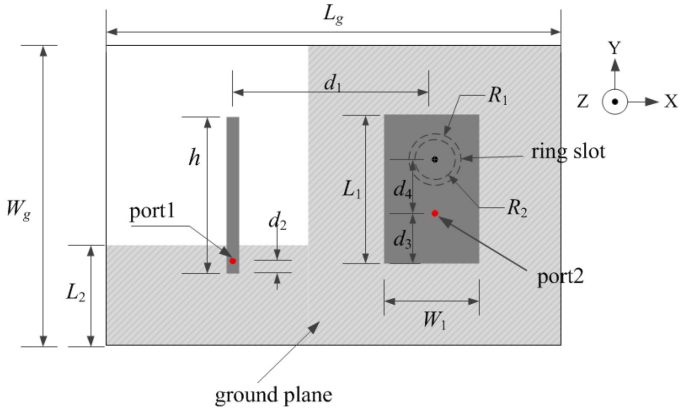

Fig. 5. The detailed geometries of the proposed monopole-patch array: h=32 mm, d_1=35 mm, L_1=30.4 mm, W_1=18 mm, L_g=60 mm, W_g=50 mm, L_2=14 mm, d_2=2 mm, d_3=10.7 mm, d_4=11.5 mm, R_1=7.5 mm, R_2=6.5 mm.

Full wave simulations were carried out in the frequency domain using CST Microwave Studio. The S-parameters of the printed monopole and the patch are shown in Fig. 6(a), both of which work well at 2.4 GHz with an isolation of above 15 dB. The individual amplitude patterns for both antennas and their amplitude ratio at the *xoz* plane are presented in Cartesian coordinates in Fig. 6(b). The pattern of the monopole is almost symmetric with respect to the $\theta = 90^\circ$ plane, whereas the patch radiates most of its power on the upper half plane, as expected. The amplitude ratio curve almost follows the trend of the cosine function, with its magnitude falling in between 0.5 and 1.3, which well fits the criteria of the amplitude ratio in section II. The RMS errors for the monopole-patch array and the array without amplitude information were calculated under a medium SNR of 10 dB, with the results presented in Fig. 6(c). The numbers of the realizations and estimations are the same as those in section II. It is observed that the maximum RMS error for the monopole-patch array is blow 1.2 degrees for all the arriving angles. Compared with the array without amplitude information, the RMS errors are reduced by 61% and 66 %, respectively, at around 90° and 270°. The phase ambiguity has been eliminated as well. In comparison with the theoretical results with optimal $m = \pm 0.611$ in Fig. 3, the RMS errors using the monopole-patch array are only slightly higher. It should be noted that the mutual distance between the antenna elements in this array is much smaller than half wavelength.

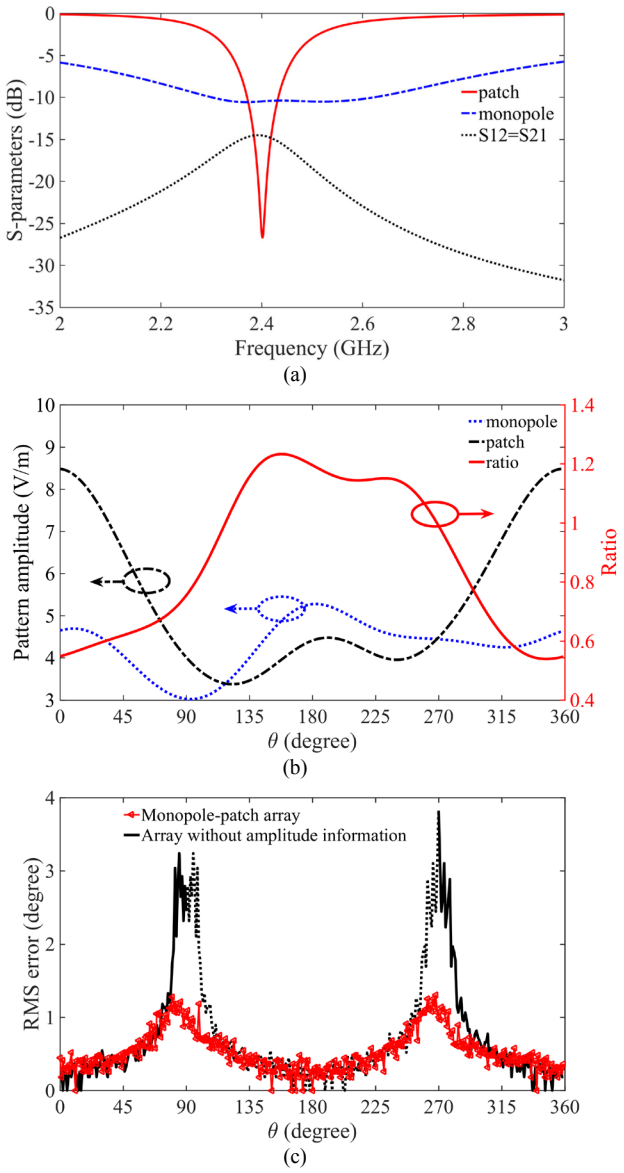

Fig. 6. (a) S-parameters of the monopole-patch array; (b) Radiation patterns and the amplitude ratio of the patterns in the $\varphi = 0^\circ$ plane (*xoz* plane); (c) RMS errors for the monopole-patch array and the array without amplitude information under the SNR of 10 dB.

One problem for the monopole-patch array is that the phase pattern of the patch on finite ground plane is not omni-directional on the $\varphi = 0^\circ$ plane. Thus, the phase difference of the signals received by the two antennas is not simply expressed as $2\pi d \sin\theta / \lambda$, but also depends on the phase pattern of the patch. To achieve good estimation accuracy, the phase pattern of the patch needs to be calibrated, which can make the measurement complicated. As opposed to the patch antenna, the phase pattern of the monopole on finite ground plane is still omni-directional. Thus, to avoid phase calibration, an asymmetrical dual-monopole array is considered for the DOA estimation.

B. Dual-monopole Array

A typical monopole as designed in Fig. 5 radiates symmetrically with respect to the ground plane. For a dual-monopole array, in order to create asymmetry in the amplitude ratio R, modifications are needed in the ground plane. To make the process more controllable, we

This article has been accepted for publication in a future issue of this journal, but has not been fully edited. Content may change prior to final publication. Citation information: DOI 10.1109/TAP.2018.2866989, IEEE Transactions on Antennas and Propagation

maintain monopole 2 as a typical monopole to keep its pattern omni-directional, and modify only monopole 1 so that the amplitude ratio is mainly governed by monopole 1. It should be noted that optimizing two antennas simultaneously may provide better results, yet it makes the procedure more complex. As we aim at validating that the proper amplitude ratio can improve the DOA estimation, efforts are not taken on giving the best monopole setup. The detailed geometries of the proposed dual-monopole array are presented in Fig. 7. For easy fabrication, the two monopoles are printed on the felt substrate with a permittivity of 1.2 and a thickness of 2 mm. The mutual distance between the two antennas is 55 mm, corresponding to 0.45λ. The ground plane is separated by a slot with d_2=2 mm, in order to enhance the isolation between the two antennas. We would like to address that the isolation is not directly related to the estimation accuracy, but high isolation is still desired since it helps to ensure the total efficiency of the antenna.

Two modifications, including adding a protruded ground plane below monopole 1 and cutting a corner from the ground plane, are made in order to achieve asymmetric radiation pattern regarding the *xoy* plane (ground plane).

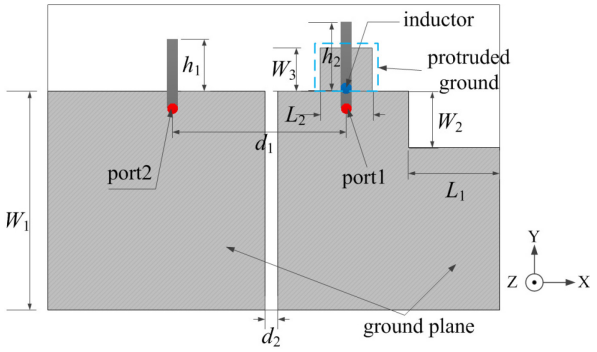

Fig. 7. The detailed geometries of the dual-monopole array: h_1=21 mm, h_2=26 mm, d_1=55 mm, d_2=2 mm, L_g=200 mm, W_g=130 mm, W_1=100 mm, W_2=25 mm, L_1=55 mm, L_2=25 mm, W_3=16 mm.

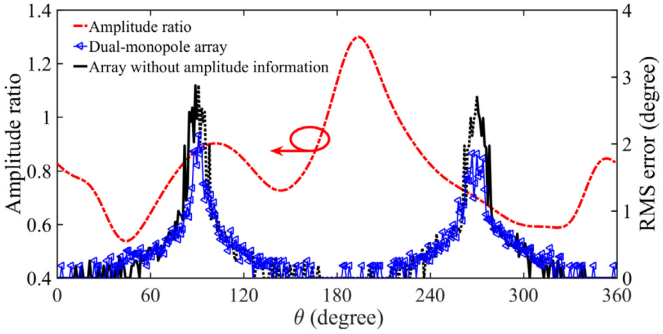

Fig. 8. Amplitude ratio of the antenna patterns and the RMS errors for the dual-monopole array and the array without amplitude information.

Fig. 8 shows the amplitude ratio of the patterns between the two monopoles. It is seen that its magnitude falls in between 0.5 and 1.4. However, the slope of the amplitude ratio is not very large at around 90°. As a result, the estimation errors increase in this area compared with those for the monopole-patch array. The RMS errors for the dual-monopole array and the array without amplitude information are also compared under the SNR of 10 dB in Fig. 8. It is seen that the phase ambiguity is successfully eliminated, yet the accuracy improvement is not as great as that of the patch-monopole array due to the reasons illustrated above. The maximum RMS errors are cut down by 24% and 40%, respectively, near 90° and 270°.

IV. Measurements

The proposed dual-monopole array was fabricated on the felt substrate with a thickness of 2 mm, as presented in Fig. 9. As in the simulation, one inductor of 2 nH was soldered near port 1. The S-parameters were measured with a vector network analyzer and shown in Fig. 10. The center frequency of the measured prototype is shifted to 2.4 GHz, which can be attributed to the fabrication tolerance of the handmade process and the permittivity of the felt substrate being different from that used in the simulation. The isolation between the antennas is above 15 dB over the operating band.

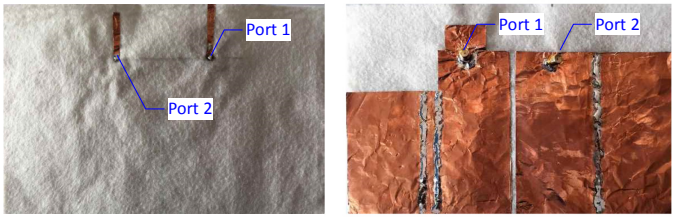

(a) (b)

Fig. 9. Prototype of the dual-monopole array for DOA estimation.

The far-field patterns on the *xoz* plane were measured at the center frequency of 2.4 GHz in an anechoic chamber. The measured and simulated results were normalized and compared in Fig. 11(a), which agree well with each other. The amplitude ratio of the measured antenna patterns is provided in Fig. 11(b), which is used to form the steering vector for the DOA estimation.

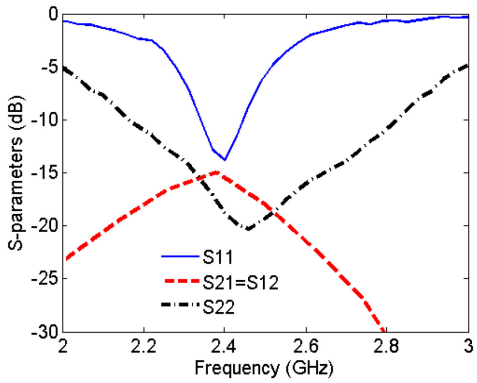

Fig. 10. Measured S-parameters of the dual-monopole array.

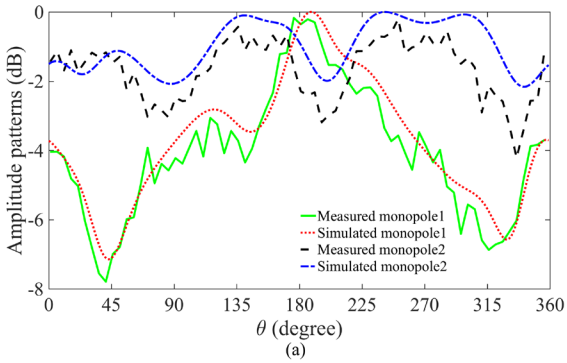

(a)

This article has been accepted for publication in a future issue of this journal, but has not been fully edited. Content may change prior to final publication. Citation information: DOI 10.1109/TAP.2018.2866989, IEEE Transactions on Antennas and Propagation

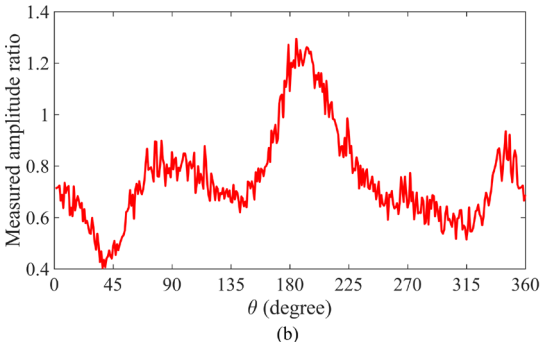

Fig.11. (a) Simulated and measured antenna patterns for the dual-monopole array in the *xoz* plane; (b) Measured amplitude ratio of the dual-monopole array.

In the DOA estimation experiment, the signal was transmitted through a horn antenna in the far-field region in the chamber, with a 15° increment each time. At each measured angle, 1500 samples were used to estimate the DOA each time, and then the errors were averaged over different estimations. Fig. 12 plots the averaged estimation errors using the MuSiC algorithm. Errors within 2° are achieved for most of the measured angles, except for 105°, where the averaged error approaches 8°. As observed from the measured amplitude ratio in Fig. 11(b), the ratio at 105° is close to that at 75°, raising the possibility of wrong estimations. By contrast, the ratios at those two angles are very different in the simulation. When averaged over all the incident angles, the estimation error is around 0.67°. If more samples were utilized in the experiment, the estimation errors could be further reduced.

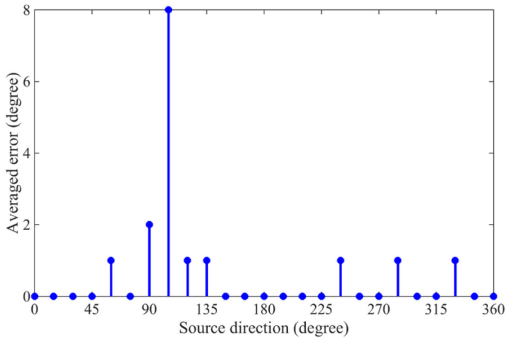

Fig. 12. Averaged errors of the DOA estimations using the dual-monopole prototype.

V. Conclusion

In this work, optimal amplitude ratio between antenna patterns has been theoretically investigated for improving DOA estimations. Following the guidance of the theoretical results, practically, two printed antenna arrays, including a monopole-patch array and a dual-monopole array have been designed to enhance the estimation accuracy in compact terminal devices. Proper asymmetries were created in the antenna patterns through structure modification, so that the amplitude information was effectively utilized to assist the DOA estimation. Both of the proposed arrays can eliminate the phase ambiguity as opposed to the conventional array using only phase information. The monopole-patch array is able to improve the accuracy by over 60% under the SNR of 10 dB, with phase calibration required in the measurement. The dual-monopole array reduces the DOA estimation errors by 20-40% without phase calibration. The prototype of the dual-monopole array was fabricated and measured in the anechoic chamber. Good estimation accuracy was achieved when the signals were transmitted through a horn antenna.

References

[1] M. Kotaru, K. Joshi, D. Bharadia and S. Katti, "SpotFi: Decimeter level localization using WiFi," in *ACM SIGCOMM Comput. Commun. Rev.*, vol. 45, no. 4, pp. 269-282, Oct. 2015.

[2] M. D. R. Islam and I. A. H. Adam, "Performance study of direction of arrival (DOA) estimation algorithms for linear array antenna," in *Proc. Int. Conf. Signal Process. Syst.*, Singapore, 2009, pp. 268-271.

[3] B. Liao, Z. G. Zhang, and S. C. Chan, "DOA estimation and tracking of ULAs with mutual coupling," *IEEE Trans. Aerosp. Electron. Syst.*, vol. 48, no. 1, pp. 891-905, Jan. 2012.

[4] H. S. Lui and H. T. Hui, "Direction-of-arrival estimation: measurement using compact antenna arrays under the influence of mutual coupling," *IEEE Antennas Propag. Mag.*, vol. 57, no. 6, pp. 62-68, Dec. 2015.

[5] E. Taillefer, A. Hirata and T. Ohira, "Direction-of-arrival estimation using radiation power pattern with an ESPAR antenna," *IEEE Trans. Antennas Propag.*, vol. 53, no. 2, pp. 678-684, Feb. 2005.

[6] C. Viswanadham, "A practical approach for controlling the shape of the radiation pattern of a microwave log-periodic antenna for wideband application," *IEEE Antennas Propag. Mag.*, vol. 56, no. 5, pp. 304-314, Oct. 2014.

[7] M. A. Al-Tarifi and D. S. Filipovic, "Amplitude-only direction finding using squinted stabilized-pattern horn antennas in W-band," in *Proc. IEEE Int. Symp. Antennas Propag. (APSURSI'2016)*, Fajardo, Puerto Rico, 2016, pp. 1183-1184.

[8] G. Lasser and D. Filipovic, "A wide-band spiral based amplitude-only azimuth direction finding system," in *Proc. IEEE Int. Symp. Antennas Propag. (APSURSI'2016)*, Fajardo, Puerto Rico, 2016, pp. 1823-1824.

[9] X. Yu, R. Zhou, H. Zhang and H. Xin, "A microwave direction of arrival estimation technique using a single antenna," *IEEE Trans. Antennas Propag.*, vol. 64, no. 7, pp. 3189-3195, Jul. 2016.

[10] J. S. Lim, G. S. Chae and Y. C. Park. "A novel technology of microwave direction finding with a combination of amplitude-measurement and phase-measurement," in *Proc. IEEE Int. Symp. Antenna Propag. (ISAP)*, Seoul, Korea, 2005, pp. 1269-1272.

[11] M. Akcakaya, C. H. Muravchik, and A. Nehorai, "Biologically inspired coupled antenna array for direction-of-arrival estimation," *IEEE Trans. Signal Process.*, vol. 59, no. 10, pp. 4795-4808, Oct. 2011.

[12] B. R. Jackson, S. Rajan, B. J. Liao and S. Wang, "Direction of arrival estimation using directive antennas in uniform circular arrays," *IEEE Trans. Antennas Propag.*, vol. 63, no. 2, pp. 736-747, Feb. 2015.

[13] M. J. Slater, C. D. Schmitz, M. D. Anderson, D. L. Jones and J. T. Bernhard, "Demonstration of an electrically small antenna array for UHF direction-of-arrival estimation," *IEEE Trans. Antennas Propag.*, vol. 61, no. 3, pp. 1371-1377, Mar. 2013.

[14] R. Zhou, H. Zhang and H. Xin, "Improved two-antenna direction finding inspired by human ears," *IEEE Trans. Antennas Propag.*, vol. 59, no. 7, pp. 2691-2697, Jul. 2011.

[15] R. Adve. ECE1515S. Lecture Notes, Topic:"Smart Antennas，" pp. 3-5, Department of Electrical and Computer Engineering, University of Toronto, Toronto, Ontario, Canada, July, 2002. [Online]. Available: http://www.comm.utoronto.ca/~rsadve/Notes/DOA.pdf

[16] X. Yang, T. Long and T. K. Sarkar, "Effect of geometry of planar antenna arrays on Cramer-Rao bounds for DOA estimation," in *Proc.10th IEEE Int. Conf. Signal Process. (ICSP 2010),* Beijing, China, 2010, pp: 389-392.

[17] M. Eric, A. Zejak, and M. Obradovic, "Ambiguity characterization of arbitrary antenna array: Type I ambiguity," in *Proc. IEEE 5th Int. Symp. Spread Spectrum Tech. Applicat.*, Sep. 1998, vol. 2, pp. 399–403.

[18] S. Sun, H. Li and J. Xiong, "Direction of arrival estimation using compact MIMO array for portable devices," in *Proc. IEEE Int. Symp. Antenna Propag. (APS 2017)*, San Diego, CA, US, 2017, pp. 1433-1434.